sustainability

MDPI

Article

Nonlinear Modelling and Control of a Power Smoothing System for a Novel Wave Energy Converter Prototype

Simon Krüner [1,*] and Christoph M. Hackl [2]

[1] Graduate Center of Engineering and Design (GC-ED), Technical University of Munich (TUM) and SINN Power GmbH, 85748 Munich, Germany
[2] Laboratory for Mechatronic and Renewable Energy Systems (LMRES), Hochschule München (HM) University of Applied Sciences, 80335 Munich, Germany
* Correspondence: simon.kruener@tum.de

Abstract: This contribution presents the control of the electrical system of a Wave Energy Converter (WEC) prototype developed by SINN Power. Due to the movement of the waves, the generated power has a very high fluctuation with a period of a few seconds. To be able to use this power, it has to be smoothed. The used Energy Storage System (ESS) is a supercapacitor bank, which is directly connected to the DC-link. Therefore, the DC-link voltage has to fluctuate according to the generated power, to charge and discharge the capacitors. The smoothed power is used to charge batteries with a DC/DC converter, which is typically used for photovoltaic applications. The DC-link voltage can be controlled with the current through the DC/DC converter, yielding a nonlinear control system where a stability analysis is carried out to prove a safe and stable operation. Measurement results at the prototype under typical sea conditions are presented, which fit the simulation results. With the presented control system, smooth power output can be guaranteed.

Keywords: Wave Energy Converter; power smoothing; energy storage system; supercapacitor bank; EDLC

Citation: Krüner, S.; Hackl, C.M. Nonlinear Modelling and Control of a Power Smoothing System for a Novel Wave Energy Converter Prototype. *Sustainability* **2022**, *14*, 13708. https://doi.org/10.3390/su142113708

Academic Editor: Nicu Bizon

Received: 9 August 2022
Accepted: 19 October 2022
Published: 22 October 2022

1. Motivation and Problem Statement

Due to the climate crisis, renewable energy resources must play a fundamental role in the future energy system. As wave energy has a higher continuity than both solar and wind energy, it has the potential to become an important part of the energy generation of tomorrow ([1] Section 2.2), [2,3].

SINN Power has developed a Wave Energy Converter (WEC) and installed their third prototype. The WEC works as a point absorber. The prototype of a single module of the power plant is mounted on the harbour wall of Heraklion on the Greek island of Crete, as shown in Figure 1. It consists of a floating buoy, a rod and generator units.

A common challenge for wave energy converters is power smoothing. The fluctuations of ocean waves range from a second-by-second basis (from wave to wave), to hourly, daily and seasonal fluctuations [4,5]. The generated electrical power fluctuates with the waves' movement and a period of a few seconds. In [6], optimal control of a WEC is proposed, where it is assumed that power smoothing is already handled internally in the mechanical or electrical power take-off components of the WEC. However, a lot of effort is required to smooth the second-by-second fluctuations. It can be shown that an arrangement of multiple WECs in a wave energy farm leads to a more uniform overall power, due to their spatial positioning and the resulting time delay of the waves at the single WEC modules [7–10]. The integration of WEC farms into offshore wind energy farms also offers strong synergies [11–13].

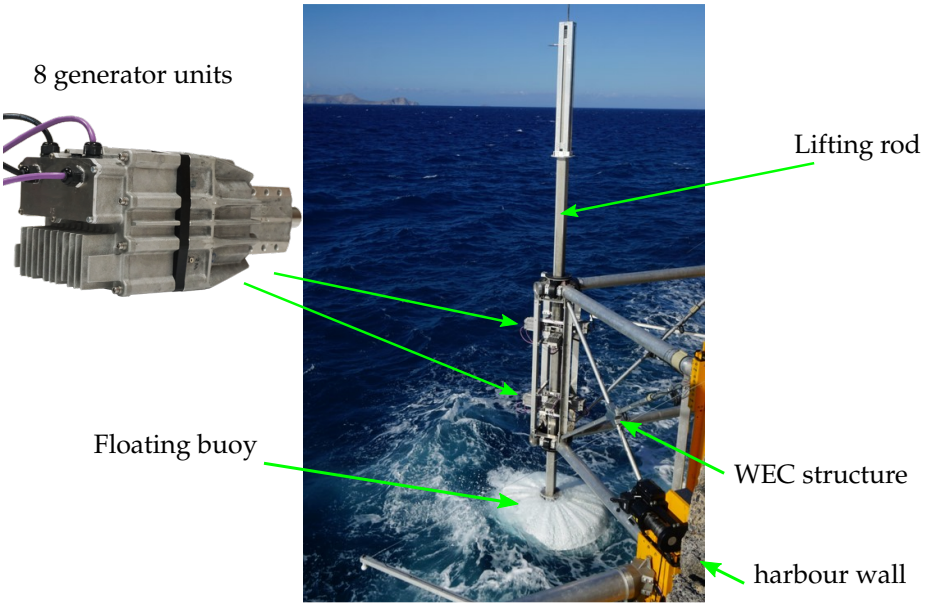

Figure 1. Picture of the WEC prototype in Crete.

Despite the general challenge of power smoothing, in particular, for the proposed novel WEC prototype, the most power is generated when the wave pushes the floating buoy upwards. In the downward movement, only the gravitation force of the floating buoy and the rod produce power. During the reversal points, where the speed is zero, the power is zero as well. Hence, the electrical power must be smoothed before it is fed into the grid. In the grid, fluctuating power could cause instability, like large voltage variations, flickers and harmonics [14–17].

To smooth this fluctuation with battery storage, it must be sized for the peak current, which can be costly. Furthermore, the very high number of cycles reduces the lifetime of the battery. When using a hybrid system consisting of batteries and supercapacitors, the battery storage can be smaller and will last longer. The supercapacitors, with their high power density, can withstand the high current peaks, while the batteries, with their high energy density, can provide or store the power over a long period of time [18–20].

In renewable energy applications, supercapacitors are used to smooth the power variations and to fulfil the grid requirements, such as the Low Voltage Ride Through (LVRT) capability [18,21,22]. In [17,23–26], different technologies such as flywheel, Superconducting Magnetic Energy Storage (SMES) and a hybrid system with a combination of flywheel and battery were considered to smooth the output power of a wave energy application.

Because of their simplicity, supercapacitors are often chosen for the short-time Energy Storage System (ESS) in WECs. In [16,27–31], the supercapacitors are connected to the DC-link with a bidirectional DC/DC converter. This allows separate control of power flow and DC-link voltage, which also leads to better utilization of the storage. In [32], a hybrid ESS with Li-ion batteries and supercapacitors is used to smooth the output power of WEC that generates a bidirectional power flow, due to its control strategy.

However, the publications mentioned above lack a detailed model and explanation of the control system for power smoothing, which will be addressed here. In this work, the supercapacitor is directly connected to the DC-link, due to its simplicity and the absence of a bidirectional DC/DC converter, at the time the prototype had to be installed. A unidirectional DC/DC converter is used to charge the battery storage.

The contributions of this paper are: (i) a detailed explanation of the electrical system of a novel full-sized WEC, (ii) introduction of a new DC-link voltage controller with the additional objective of power smoothing; furthermore, (iii) derivation of a nonlinear state-space model, (iv) a stability analysis is conducted to proof a safe and reliable operation, (v) validation by real measurement results at the prototype under harsh sea conditions and

(vi) comparison of the measurement results with the simulation to prove the correctness of the model.

In the following, the control of the electrical system of the single WEC module is presented. First, the electrical system with its components will be explained, followed by a stability analysis in Section 4. Section 3 describes how the power smoothing is done and how the control of the DC-link works. Finally, in Section 5, the measurement results are presented and compared to the simulation results.

2. Electrical System of the Wave Energy Converter

Figure 2 shows the simplified schematic of the WEC's electrical system as it is realised at the test site. The supercapacitor bank and the DC/DC converter are described in more detail in the following.

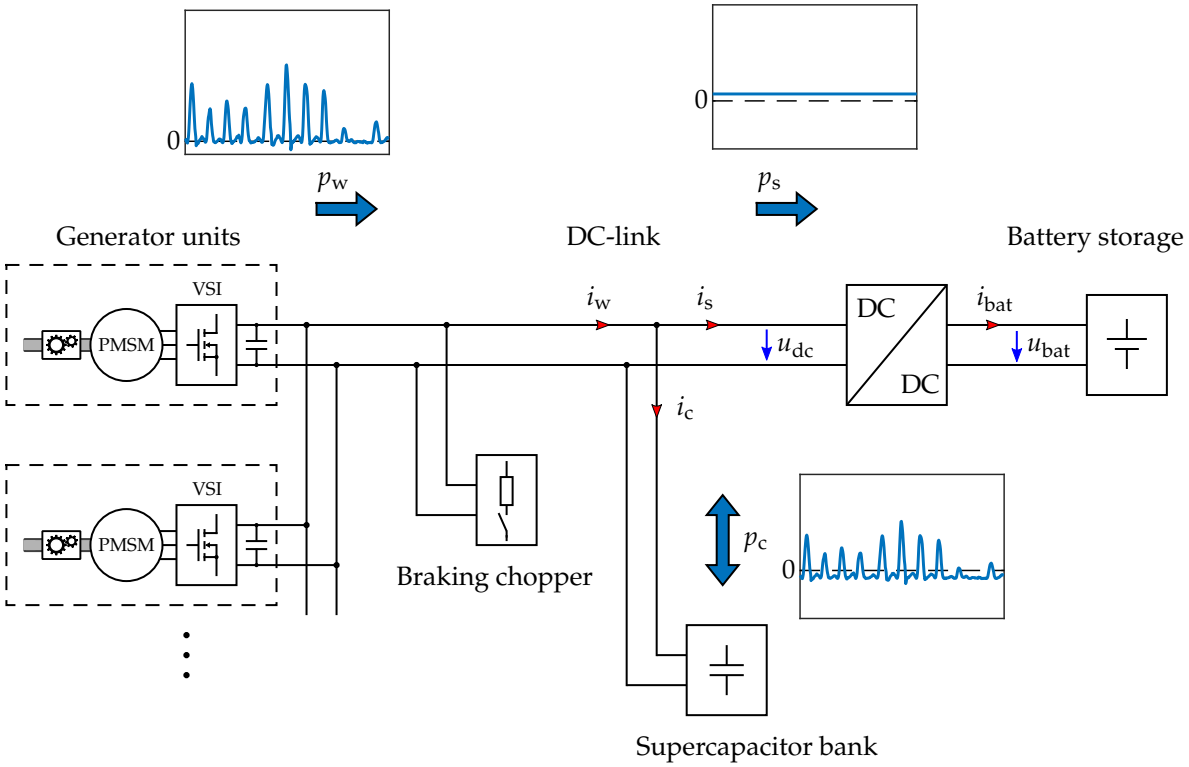

Figure 2. Simplified schematic of the electrical system of the wave energy converter and illustration of the power flow, where p_w is the fluctuating power from the WEC, p_c is the power flowing in and out of the supercapacitors and p_s is the smoothed power flow to the battery.

The generated energy is used to charge batteries. This allows for more flexibility and is more tolerant to fluctuations, which can occur during the tests of different control strategies. The energy in the batteries is used for various peripherals, which ensures that the batteries do not become fully charged, so that the energy generated by the WEC can always be stored. The charging is done by means of a unidirectional DC/DC converter, connected to the DC-link.

Power smoothing requires energy storage that stores the power peaks in the upwards movement and releases it during time periods of less power generation. Here, a supercapacitor bank is used, which is directly connected in parallel to the DC-link.

A braking chopper is integrated as a safety measure to dissipate excess energy. This prevents the voltage to rise over a specified limit. The chopper works completely independently and is therefore considered a disturbance to the control system. Moreover, if the control system is working correctly, the chopper does not need to intervene.

2.1. Generator Units

The floating buoy of the WEC swims on the water and moves up and down with each wave. The rod is attached to the buoy and moves with it. Over the rolls of multiple generator units, which are pressed on the rod with springs, the vertical movement is converted into a rotary movement. The main components of the generator unit are a gearbox, a Permanent-Magnet Synchronous Machine (PMSM), and a Voltage Source Inverter (VSI). The rated power of one generator unit is about 3 kW.

The current through the PMSM is controlled by the VSI, which allows the torque of the generator rolls to be controlled. Thus, the mechanical power can be converted into electrical power by braking the movement of the rod. All DC outputs of the generator units are connected in parallel to the DC-link, which is also the connection to the shore.

The maximum allowed DC-link voltage is 400 V, due to the voltage rating of the electrical components in the VSI. For additional safety, the voltage is limited to $u_{\mathrm{dc,max}} = 380$ V. The VSI requires minimal voltage for the current control, which is related to the rotational speed of the PMSM. Here, the voltage should not fall below $u_{\mathrm{dc,min}} = 300$ V. The nominal voltage is $u_{\mathrm{dc,nom}} = 350$ V.

The generator unit and the implemented current control were presented and optimized in a previous work [33].

2.2. Supercapacitor Bank

A supercapacitor, also called an ultracapacitor or Electric Double-Layer Capacitor (EDLC), is characterized by its very high capacitance, reaching up to several 1000 F. Consequently, the voltage rating is rather low, typically under 3 V. The electrical parameters of the used supercapacitor cell are listed in Table 1.

Table 1. Eletrical parameters of the used supercapacitor cell, produced by Maxwell Technologies [34].

Electrical Parameter	Symbol	Value
Rated Capacitance	C_i	350 F
Equivalent Series Resistor	$R_{\mathrm{esr},i}$	3.2 mΩ
Rated Voltage	$U_{\mathrm{nom},i}$	2.7 V
Absolute Maximum Voltage	$U_{\mathrm{max},i}$	2.85 V
Absolute Maximum Current	$I_{\mathrm{max},i}$	170 A
Maximum Leakage Current	$I_{\mathrm{leak},i}$	0.30 mA

To achieve more dielectric strength, the capacitors can be connected in series. Due to component tolerances and ageing, different voltages can occur at the single capacitors during charging and discharging. Hence, to avoid overvoltage, the cells must be balanced [35,36].

Here, the maximum allowed DC-link voltage u_{dc} is 400 V. Therefore, at least 149 cells in series are necessary. The developed supercapacitor bank consists of $N_{\mathrm{c}} = 160$ in series connected cells, divided into 16 modules with 10 cells each.

The balancing of the cells is achieved by a parallel connection of a balancing circuit to each cell. It consists of a resistor and a serially connected bipolar transistor. An analogue circuit compares the voltage of two consecutive cells and uses the transistor to control the current through the resistor. The supercapacitor bank is shown in Figure 3.

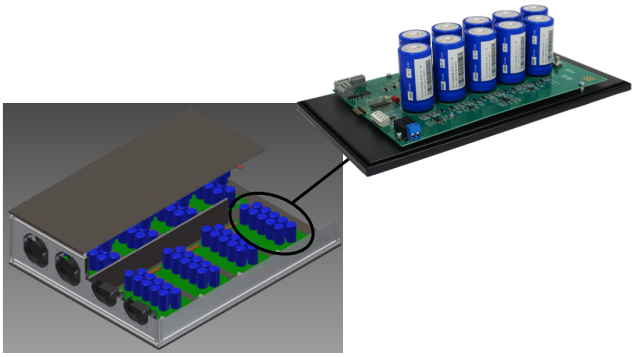

Figure 3. CAD figure of the supercapacitor bank with a photograph of one supercapacitor module of the prototype.

The bank is modelled as an RC model, as shown in Figure 4. More detailed models, such as the RC parallel branch model, are not considered, as the dynamic behaviour of the RC model is sufficient for this case [37,38]. The current induced by self-discharging and balancing is neglected in the model, as it occurs over a longer period of time during which several waves appear, and is, therefore, not relevant to the dynamic behaviour.

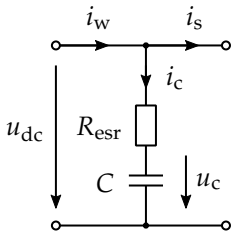

Figure 4. Equivalent circuit of the supercapacitor bank.

Due to the series connection of the cells, the equivalent series resistors $R_{esr,i}$ of each cell are summed up, resulting in the overall resistance

$$R_{esr} = \sum_{i=1}^{N_c} R_{esr,i}\,. \tag{1}$$

The overall capacitance C is given by

$$C = \frac{1}{\sum\limits_{i=1}^{N_c} \frac{1}{C_i}}\,. \tag{2}$$

Assuming that each cell has the same capacitance, the calculation can be simplified to

$$C = \frac{C_i}{N_c}\,. \tag{3}$$

The VSI of the generator units has a DC-link capacitor to stabilize the voltage at their terminals. However, they are very small compared to the capacitance of the supercapacitor bank and can be neglected. The other parameters are calculated in the same way, leading to the electrical parameters of the supercapacitor bank, listed in Table 2.

Table 2. Electrical parameters of a supercapacitor bank.

Electrical Parameter	Symbol	Value
Rated Capacitance	C	2.19 F
Equivalent Series Resistor	R_{esr}	512 mΩ
Rated Voltage	U_{nom}	432 V
Absolute Maximum Voltage	U_{max}	456 V
Absolute Maximum Current	I_{max}	170 A

Due to the limits of the DC-link voltage u_{dc}, the stored energy in the supercapacitors cannot be utilized entirely. The maximally available energy is

$$\Delta E_{c,max} = \frac{1}{2} C \left(u_{dc,max}^2 - u_{dc,min}^2 \right) \approx 16.5 \text{ Wh}, \quad (4)$$

which can be used for power smoothing and represent about 38% of the possibly stored energy. There are several methods to estimate the necessary storage size [27,39,40]. For a rough estimation, it is assumed that the WEC produces the maximal power over 2 s, which is a typical duration of a power pulse. In the prototype, 8 generator units with a rated power of 3 kW are installed. To estimate the worst case, it is assumed that all generators deliver their rated power over two seconds. Subtracting a realistic average power of 3 kW for this condition results in energy of about 12 Wh, which can be covered by the installed supercapacitor bank (see Equation (4)). This energy needs to be stored during the assumed two seconds and is then continuously discharged until the next wave arrives. Thus, a power fluctuation of about 7 times the average power can be suppressed.

2.3. DC/DC Converter

Figure 5a shows the DC/DC converter VarioString VS-70, made by Studer Innotec, which is used to charge 48-V-batteries from the DC-link. The VarioString is designed to be installed in a photovoltaic application, however, the specifications, listed in Table 3, are perfectly suited for the application considered here. The very high efficiency is made possible by an LLC resonant half-bridge topology, shown in Figure 5b. This topology allows Zero Voltage Switching (ZVS), which leads to very low switching losses [41].

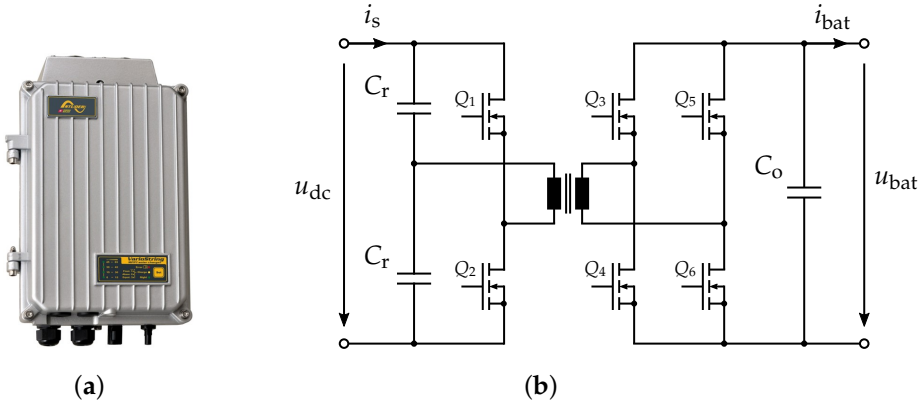

Figure 5. (**a**) Picture of the DC/DC converter VarioString VS-70 and (**b**) LLC resonant topology of the VarioString VS-70 DC/DC converter with a split resonant capacitor technique.

The DC/DC converter can be configured to operate current controlled, which allows us to control the current i_s. The reference value $i_{s,ref}$ is transmitted over a serial RS-232 communication bus from a Programmable Logic Control (PLC), where the control of the DC-link is implemented. The PLC, made by B&R, can measure the currents and voltages in the system, as well as the waves' elevation and the position of the floating buoy.

Table 3. Eletrical parameters of the VarioString VS-70 [42].

Electrical Parameter	Symbol	Value
Maximum Input Power	$P_{s,max}$	4.2 kW
Maximum Input Voltage	$U_{s,max}$	600 V
Maximum Input Current	$I_{s,max}$	13 A
Nominal Battery Voltages	$U_{bat,nom}$	48 V
Maximum Battery Current	$I_{bat,max}$	70 A
Maximum Efficiency	η	>98%

3. Control of the DC-Link

The control of the DC-link has to fulfil two objectives. On one hand, the battery current i_{bat} should be as constant as possible to increase the lifetime of the battery [43]. On the other hand, the DC-link voltage should remain within the limits and keep the nominal value on average. In this case, the nominal voltage $u_{dc,nom} = 350$ V is chosen, see Section 2.1. Hence, the amount of stored energy from the nominal voltage to the upper voltage limit is approximately the same as from the nominal voltage to the lower voltage limit.

The stored energy

$$E_c = \frac{1}{2} C u_c^2 \tag{5}$$

in the capacitor bank is proportional to the square of the capacity voltage u_c. That means, if energy needs to be stored, the DC-link voltage u_{dc} must increase. If the energy should be reduced, the voltage must decrease.

The DC-link voltage

$$u_{dc} = u_{esr} + u_c = R_{esr}\, i_c + \frac{1}{C} \int i_c \, dt + u_{c,0} \tag{6}$$

results from the current i_c through the capacitor bank. The voltage $u_{c,0}$ is the initial voltage over the capacitance C at $t = 0$.

The DC-Link voltage u_{dc} can be controlled with the current

$$i_s = i_w - i_c \tag{7}$$

flowing into the energy storage system through the DC/DC converter. The current i_w from the WEC is interpreted as a disturbance. The dynamics of the DC/DC converter are approximated by a first-order transfer function with the time constant τ_s. Experiments in the laboratory showed, that this assumption describes the behaviour sufficiently well. The dynamic of the DC-link voltage can be described by

$$\frac{u_{dc}(s)}{i_{s,ref}(s)} = -\frac{1 + s\, R_{esr}\, C}{s\, C(1 + s\, \tau_s)}. \tag{8}$$

The system shows an integral behaviour, so that a proportional (P) controller would be sufficient. However, since the disturbing current i_w is acting on the system, still, a stationary control deviation can occur. This can be compensated for by a controller with integral control action ([44], Section 7), resulting in a Proportional-Integral (PI) controller with transfer function

$$\frac{i_{s,ref}(s)}{u_{dc,ref}(s) - u_{dc}(s)} = V_r \frac{1 + s\, \tau_r}{s\, \tau_r}. \tag{9}$$

Due to the double integrator, the controller is tuned according to the Symmetrical Optimum (SO) to achieve a maximum phase margin ([45], Section 1.3.2), which yields

$$V_\mathrm{r} = -\frac{C}{2\,\tau_\mathrm{s}} \quad \text{and} \quad \tau_\mathrm{r} = 4\,\tau_\mathrm{s}\,. \tag{10}$$

The control of the DC-link voltage u_dc allows now to control the energy in the supercapacitor bank, see Equation (5). To keep the battery current i_bat constant, the power p_s through the DC/DC converter must be constant as well. This power is converted to the lower voltage level u_bat of the batteries. Since the battery voltage is nearly constant, the constant power flow implies a constant charging current of the batteries. Hence, the power p_s should be the average of the generated power p_w. Filtering the generated power p_w with a low pass filter, which has a very low cutoff frequency, gives the averaged power $\overline{p}_\mathrm{w}$. The desired power $p_\mathrm{c,ref}$ through the capacitance of the bank can be calculated as

$$p_\mathrm{c,ref} = p_\mathrm{w} - \overline{p}_\mathrm{w} - p_\mathrm{esr}\,, \tag{11}$$

where

$$p_\mathrm{esr} = R_\mathrm{esr}\,i_\mathrm{c}^2 \tag{12}$$

is the dissipated power in the equivalent series resistor R_esr. With the nonlinear differential equation

$$\frac{\mathrm{d}}{\mathrm{d}t}u_\mathrm{c,ref} = \frac{1}{C}\,\frac{p_\mathrm{c,ref}}{u_\mathrm{c,ref}}\,, \tag{13}$$

the desired voltage over the capacitance C can be calculated. To control the voltage u_c, a feedforward control is required, which is achieved by adding the voltage u_esr to the reference voltage $u_\mathrm{c,ref}$, yielding the reference DC-link voltage

$$u_\mathrm{dc,ref} = u_\mathrm{c,ref} + u_\mathrm{esr} = u_\mathrm{c,ref} + R_\mathrm{esr}\,i_\mathrm{c}\,. \tag{14}$$

This feedforward control with the voltage u_esr over the ESR of the supercapacitors allows us to control the voltage u_c and thus direct control of the stored energy in the supercapacitor bank.

A restoring current i_res is introduced, which should cause the voltage to fluctuate around the nominal value on average. Otherwise, the voltage would drift away. If energy should be stored in the supercapacitors ($p_\mathrm{w} > p_\mathrm{s}$) and the DC-link voltage is already above the nominal voltage ($u_\mathrm{c,ref} > u_\mathrm{dc,nom}$), then the power p_s through the DC/DC converter should increase. If energy is required ($p_\mathrm{w} < p_\mathrm{s}$) and the DC-link voltage is below the nominal voltage ($u_\mathrm{c,ref} < u_\mathrm{dc,nom}$), then p_s should decrease. The restoring current is defined as

$$i_\mathrm{res} := \begin{cases} -V_\mathrm{res}(u_\mathrm{c,ref} - u_\mathrm{dc,nom})\,, \\ \qquad\qquad \text{if} \quad p_\mathrm{w} > p_\mathrm{s} \;\wedge\; u_\mathrm{c,ref} > u_\mathrm{dc,nom} \\ \qquad\qquad \text{or} \quad p_\mathrm{w} < p_\mathrm{s} \;\wedge\; u_\mathrm{c,ref} < u_\mathrm{dc,nom} \\ 0\,, \qquad\quad \text{otherwise.} \end{cases} \tag{15}$$

In Figure 6, the block diagram of the whole control system is shown. The restoring current is added to the reference current $i_\mathrm{c,ref}$ before the integrator, which leads to an integrating, as well as a filtering behaviour of this restoring term. The crossover frequency of the transfer function

$$\frac{u_\mathrm{c,ref}(s)}{u_\mathrm{c,ref}(s) - u_\mathrm{dc,nom}(s)} = -\frac{V_\mathrm{res}}{s\,C} \tag{16}$$

is given by

$$f_{\mathrm{res}} = \frac{V_{\mathrm{res}}}{2\pi C}\,, \tag{17}$$

which yields the proportional gain V_{res}. The crossover frequency is set to one-tenth of the lowest frequency of the waves, which can occur, which is approximately 0.15 Hz.

Finally, the resulting voltage is limited to the desired operating range. This ensures, that the DC-link voltage does not exceed the limits, even if more energy needs to be stored due to very high power peaks. The fast voltage control loop guarantees, that this excess energy is fed directly into the batteries. The alternative would be to have it dissipated by the braking chopper, which should be avoided, as it would lead to efficiency loss.

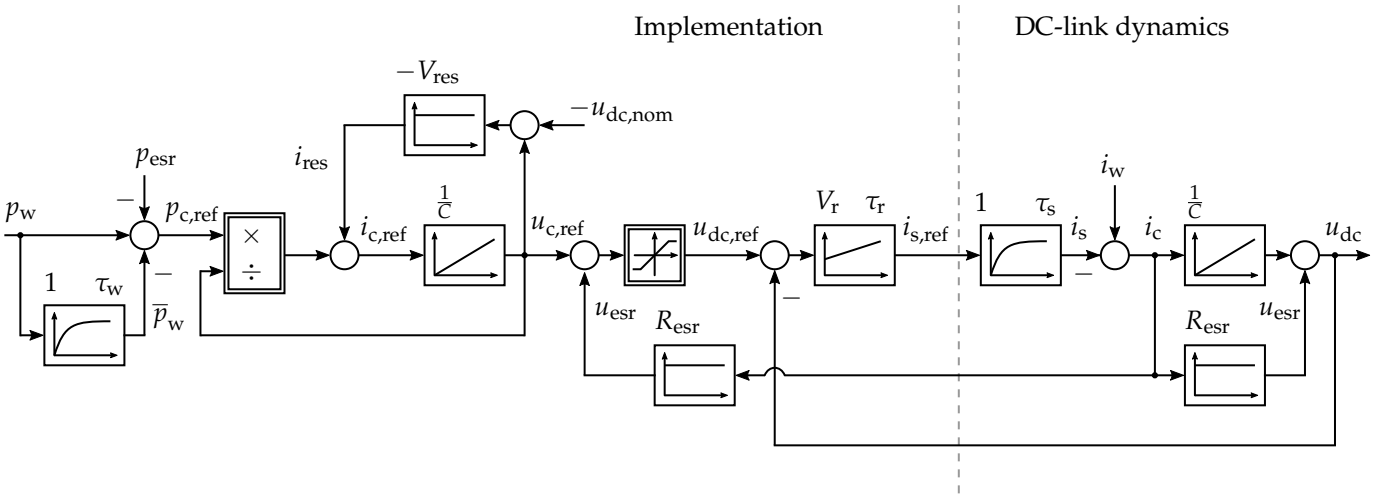

Figure 6. Block diagram of the voltage control loop for power smoothing.

4. Stability Analysis

To prove the stability of the nonlinear control system with multiple feedback, a stability analysis is conducted in the state space. The nonlinear dynamics of the system are given by

$$\left.\begin{aligned}
\frac{\mathrm{d}}{\mathrm{d}t}u_{\mathrm{c}} &= \frac{1}{C}\left(i_{\mathrm{w}} - i_{\mathrm{s}}\right)\\
\frac{\mathrm{d}}{\mathrm{d}t}i_{\mathrm{s}} &= \frac{1}{\tau_{\mathrm{s}}}\left[V_{\mathrm{r}}\left(\underbrace{f_{\mathrm{sat}}\left(u_{\mathrm{dc,min}},\, u_{\mathrm{c,ref}} + R_{\mathrm{esr}}\, i_{\mathrm{c}},\, u_{\mathrm{dc,max}}\right)}_{=u_{\mathrm{dc,ref}}} - \underbrace{\left(u_{\mathrm{c}} + R_{\mathrm{esr}}\, i_{\mathrm{c}}\right)}_{=u_{\mathrm{dc}}}\right) + \xi_{\mathrm{s,ref}} - i_{\mathrm{s}}\right]\\
\frac{\mathrm{d}}{\mathrm{d}t}\xi_{\mathrm{s,ref}} &= \frac{V_{\mathrm{r}}}{\tau_{\mathrm{r}}}\left(\underbrace{f_{\mathrm{sat}}\left(u_{\mathrm{dc,min}},\, u_{\mathrm{c,ref}} + R_{\mathrm{esr}}\, i_{\mathrm{c}},\, u_{\mathrm{dc,max}}\right)}_{=u_{\mathrm{dc,ref}}} - \underbrace{\left(u_{\mathrm{c}} + R_{\mathrm{esr}}\, i_{\mathrm{c}}\right)}_{=u_{\mathrm{dc}}}\right)\\
\frac{\mathrm{d}}{\mathrm{d}t}u_{\mathrm{c,ref}} &= \frac{1}{C}\left(\frac{p_{\mathrm{w}} - \overline{p}_{\mathrm{w}} - p_{\mathrm{esr}}}{u_{\mathrm{c,ref}}}\,\underbrace{-V_{\mathrm{res}}\left(u_{\mathrm{c,ref}} - u_{\mathrm{dc,nom}}\right)}_{=i_{\mathrm{res}}}\right)\\
\frac{\mathrm{d}}{\mathrm{d}t}\overline{p}_{\mathrm{w}} &= \frac{1}{\tau_{\mathrm{w}}}\left(p_{\mathrm{w}} - \overline{p}_{\mathrm{w}}\right),
\end{aligned}\right\} \tag{18}$$

where the state $\xi_{s,ref}$ is introduced to represent the integral action of the PI-controller. The saturation f_{sat} is defined by

$$f_{sat}(x_{min}, x, x_{max}) := \begin{cases} x_{min}, & x \leq x_{min} \\ x, & x_{min} < x < x_{max} \\ x_{max}, & x \geq x_{max}\,. \end{cases} \tag{19}$$

For the system to be analysed for stability, it must be linearised around the operation point. Since the operational DC-link voltage lies between the limits $u_{dc,min}$ and $u_{dc,max}$, the saturation f_{sat} can be neglected, yielding

$$\left.\begin{aligned} \frac{\mathrm{d}}{\mathrm{d}t} i_s &= \frac{1}{\tau_s}\left[V_r(u_{c,ref} - u_c) + \xi_{s,ref} - i_s\right] \\ \frac{\mathrm{d}}{\mathrm{d}t}\xi_{s,ref} &= \frac{V_r}{\tau_r}(u_{c,ref} - u_c)\,. \end{aligned}\right\} \tag{20}$$

Notice, that u_{esr} and R_{esr} do not appear in (20), as they are compensated for by feedforward control. Only the dissipated power p_{esr} remains in the dynamic of $u_{c,ref}$, which must be subtracted from the incoming power p_w of the WEC, as it is dissipated at the equivalent series resistor R_{esr} and cannot be used.

Furthermore, the expressions of the powers in (18) are replaced by the multiplication of their corresponding current and voltage. It is assumed that the averaged DC-link voltage $\overline{u}_{dc}$ and the operation point $u^\star_{dc}$ are constant and correspond to its nominal value $u_{dc,nom}$, which is reasonable as the DC-link voltage u_{dc} changes little compared to the current i_w from the WEC, as it can be seen from the results. The nonlinear dynamics of the reference voltage $u_{c,ref}$ and the averaged input current $\bar{i}_w$ are then given as follows

$$\left.\begin{aligned} \frac{\mathrm{d}}{\mathrm{d}t} u_{c,ref} &= \frac{1}{C}\left[\frac{u_{dc,nom}(i_w - \bar{i}_w) - R_{esr}(i_w - i_s)^2}{u_{c,ref}} - V_{res}(u_{c,ref} - u_{dc,nom})\right] \\ \frac{\mathrm{d}}{\mathrm{d}t}\bar{i}_w &= \frac{1}{\tau_w}\left[i_w - \bar{i}_w\right]. \end{aligned}\right\} \tag{21}$$

Linearization around the operation point $\boldsymbol{x}^\star := (u_c^\star, i_s^\star, \xi_{s,ref}^\star, u_{c,ref}^\star, \bar{i}_w^\star)^\top$ yields the small signal state space representation of the DC-link control system as follows

$$\left.\begin{aligned} \frac{\mathrm{d}}{\mathrm{d}t}\underbrace{\begin{pmatrix} \Delta u_c \\ \Delta i_s \\ \Delta\xi_{s,ref} \\ \Delta u_{c,ref} \\ \Delta\bar{i}_w \end{pmatrix}}_{:=\boldsymbol{x}} &= \underbrace{\begin{bmatrix} 0 & -\frac{1}{C} & 0 & 0 & 0 \\ -\frac{V_r}{\tau_s} & -\frac{1}{\tau_s} & \frac{1}{\tau_s} & \frac{V_r}{\tau_s} & 0 \\ -\frac{V_r}{\tau_r} & 0 & 0 & \frac{V_r}{\tau_r} & 0 \\ 0 & \frac{2\,R_{esr}\,(i_w^\star - i_s^\star)}{C\,u_{c,ref}^\star} & 0 & \alpha_{44} & -\frac{u_{dc,nom}}{C\,u_{c,ref}^\star} \\ 0 & 0 & 0 & 0 & -\frac{1}{\tau_w} \end{bmatrix}}_{:=\boldsymbol{A}} \begin{pmatrix} \Delta u_c \\ \Delta i_s \\ \Delta\xi_{s,ref} \\ \Delta u_{c,ref} \\ \Delta\bar{i}_w \end{pmatrix} + \underbrace{\begin{pmatrix} \frac{1}{C} \\ 0 \\ 0 \\ \frac{u_{dc,nom} - 2\,R_{esr}\,(i_w^\star - i_s^\star)}{C\,u_{c,ref}^\star} \\ \frac{1}{\tau_w} \end{pmatrix}}_{:=\boldsymbol{B}} \Delta i_w \\ \underbrace{\begin{pmatrix} i_s \\ u_{dc} \end{pmatrix}}_{:=\boldsymbol{y}} &= \underbrace{\begin{bmatrix} 0 & 1 & 0 & 0 & 0 \\ 1 & -R_{esr} & 0 & 0 & 0 \end{bmatrix}}_{:=\boldsymbol{C}} \begin{pmatrix} \Delta u_c \\ \Delta i_s \\ \Delta\xi_{s,ref} \\ \Delta u_{c,ref} \\ \Delta\bar{i}_w \end{pmatrix} + \begin{pmatrix} 0 \\ R_{esr} \end{pmatrix} \Delta i_w\,, \end{aligned}\right\} \tag{22}$$

with the coefficient

$$\alpha_{44} = -\frac{1}{C}\left(\frac{u_{\mathrm{dc,nom}}\,(i_{\mathrm{w}}^{\star} - \bar{i}_{\mathrm{w}}) - R_{\mathrm{esr}}\,(i_{\mathrm{w}}^{\star} - i_{\mathrm{s}}^{\star})^2}{(u_{\mathrm{c,ref}}^{\star})^2} + V_{\mathrm{res}}\right). \tag{23}$$

A Linear Time-Invariant (LTI) system is exponentially stable if and only if its characteristic polynomial $\chi_A(s)$ a Hurwitz polynomial, which here is given as

$$\chi_A(s) = \det(s\boldsymbol{I} - \boldsymbol{A}) = \frac{1}{\tau_{\mathrm{w}}}(1 + s\,\tau_{\mathrm{w}})\left(a_0 + s\,a_1 + s^2\,a_2 + s^3\,a_3 + s^4\,a_4\right), \tag{24}$$

with

$$\left.\begin{aligned} a_0 &= \frac{V_{\mathrm{r}}\,\alpha_{44}}{C\,\tau_{\mathrm{r}}\,\tau_{\mathrm{s}}} \\ a_1 &= \frac{-V_{\mathrm{r}}}{C\,\tau_{\mathrm{s}}}\left(\frac{1}{\tau_{\mathrm{r}}} - \alpha_{44} + \frac{2\,R_{\mathrm{esr}}\,(i_{\mathrm{w}}^{\star} - i_{\mathrm{s}}^{\star})}{\tau_{\mathrm{r}}\,u_{\mathrm{c,ref}}}\right) \\ a_2 &= \frac{-V_{\mathrm{r}}}{C\,\tau_{\mathrm{s}}} - \frac{\alpha_{44}}{\tau_{\mathrm{s}}} + \frac{-V_{\mathrm{r}}}{\tau_{\mathrm{s}}}\,\frac{2\,R_{\mathrm{esr}}\,(i_{\mathrm{w}}^{\star} - i_{\mathrm{s}}^{\star})}{C\,u_{\mathrm{c,ref}}} \\ a_3 &= \frac{1}{\tau_{\mathrm{s}}} - \alpha_{44} \\ a_4 &= 1\,. \end{aligned}\right\} \tag{25}$$

The term $\frac{1}{\tau_{\mathrm{w}}}(1 + s\,\tau_{\mathrm{w}})$ can be factored out. It is stable for all $\tau_{\mathrm{w}} > 0$ and therefore does not have to be considered for the stability analysis, which reduces the order of the polynomial to four. According to the Hurwitz criterion, the system is stable if ([44] Section 5.4.2)

(i) all coefficients a_i are positive (i.e., $a_i > 0$ for $i \in \{1, 2, \ldots\}$) and
(ii) all leading principal minors D_i of the Hurwitz matrix are positive.

Due to the redundancy of the Hurwitz criterion and according to the Liénard-Chipart criterion, for a fourth-order polynomial, it is sufficient to evaluate only the leading principal minors

$$\left.\begin{aligned} D_1 &= a_1 \qquad \text{and} \\ D_3 &= a_1\,a_2\,a_3 - a_1^2\,a_4 - a_0\,a_3^2 \end{aligned}\right\} \tag{26}$$

for positivity in addition to the coefficients a_i ([46] Section 3.4.5).

The determinate D_3 also leads to a fourth-order polynomial in the arguments $i_{\mathrm{w}}^{\star}$, $i_{\mathrm{s}}^{\star}$ and $u_{\mathrm{c,ref}}^{\star}$ (due to squaring of α_{44}), which is why a numerical approach is chosen to prove the positivity for various operation points. Therefore, the physical constraints are included and used accordingly to account for the worst-case. Figure 7 shows the coefficients a_0 to a_3 and the determinant D_3 over the input operational current $i_{\mathrm{w}}^{\star}$ and for two different reference voltages $u_{\mathrm{c,ref}}^{\star} = u_{\mathrm{dc,min}}$ and $u_{\mathrm{c,ref}}^{\star} = u_{\mathrm{dc,max}}$. Further analysis shows, that the worst-case of stability is if the reference voltage $u_{\mathrm{c,ref}}^{\star}$ is set to the minimum DC-link voltage $u_{\mathrm{dc,min}}$, the current $i_{\mathrm{s}}^{\star}$ flowing into the DC/DC converter is set to $I_{\mathrm{s,max}}$ and the current $\bar{i}_{\mathrm{w}}^{\star}$ is set to zero, which is shown by the blue curves in Figure 7.

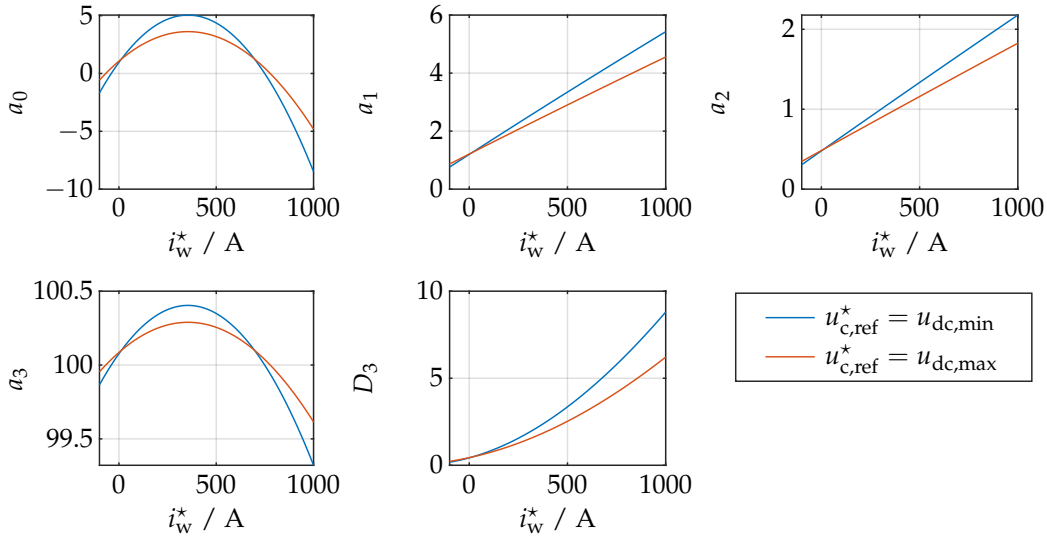

Figure 7. Numerical stability analysis of the coefficients a_0 to a_3 and the determinant D_3 over the input operational current $i_w^\star$ and for two different reference voltages $u_{c,ref}^\star = u_{dc,min}$ [——] and $u_{c,ref}^\star = u_{dc,max}$ [——], where $u_{c,ref}^\star = u_{dc,min}$ accounts for the worst-case.

Each value is positive at least in the range $-40\ \text{A} < i_w^\star < 700\ \text{A}$. Physically, it is impossible for these limits to be exceeded, which is why the analysed system is exponentially stable.

5. Results

In this section, the results of the DC-link control are presented, where the measured quantities under typical sea conditions are compared to the simulated ones. The measured current i_w and power p_w of the generator units are used as inputs for the simulation.

Figure 8 shows the results, beginning with the relative rod position h_w at the top, to illustrate the movement of the point absorber. A laser sensor, mounted on the WEC structure, measures the distance to a reflector on the lifting rod. The analogue signal from the sensor is connected to the PLC, which converts and records all data. The next subplot shows the currents, where the blue line is the measured current i_w, coming from the generator units. The red line is the measured current i_s and the yellow line is the simulated current i_s. The currents are measured indirectly via shunt resistors. The voltage over the shunt resistor is connected via an operational amplifier circuit to the PLC.

In the third subplot, the DC-link voltage u_{dc} is shown, where, as before, the red signal is the measured voltage and the yellow signal is the simulated voltage. The voltage u_{dc} is also measured and fed to the PLC via an operational amplifier circuit. At the bottom, the power p_w of the generator units and the resulting smoothed power p_s from the measurement and the simulation are shown.

The measurement was made, when the generated power was very high and the significant wave period with about 5 s was very short, as this is the most challenging condition for power smoothing. The peaks in the current i_w from the generator units occur when the rod is moving upwards. This is where the most power is produced, as seen in the last subplot. The shapes of the currents and the corresponding powers are very similar. This is due to the high capacitance, so the change in the DC voltage does not significantly affect the power. Thus, the power is mainly determined by the current. The measured, smoothed power p_s fluctuates slightly more than the simulated one. This is mainly caused by parameter uncertainties and noise.

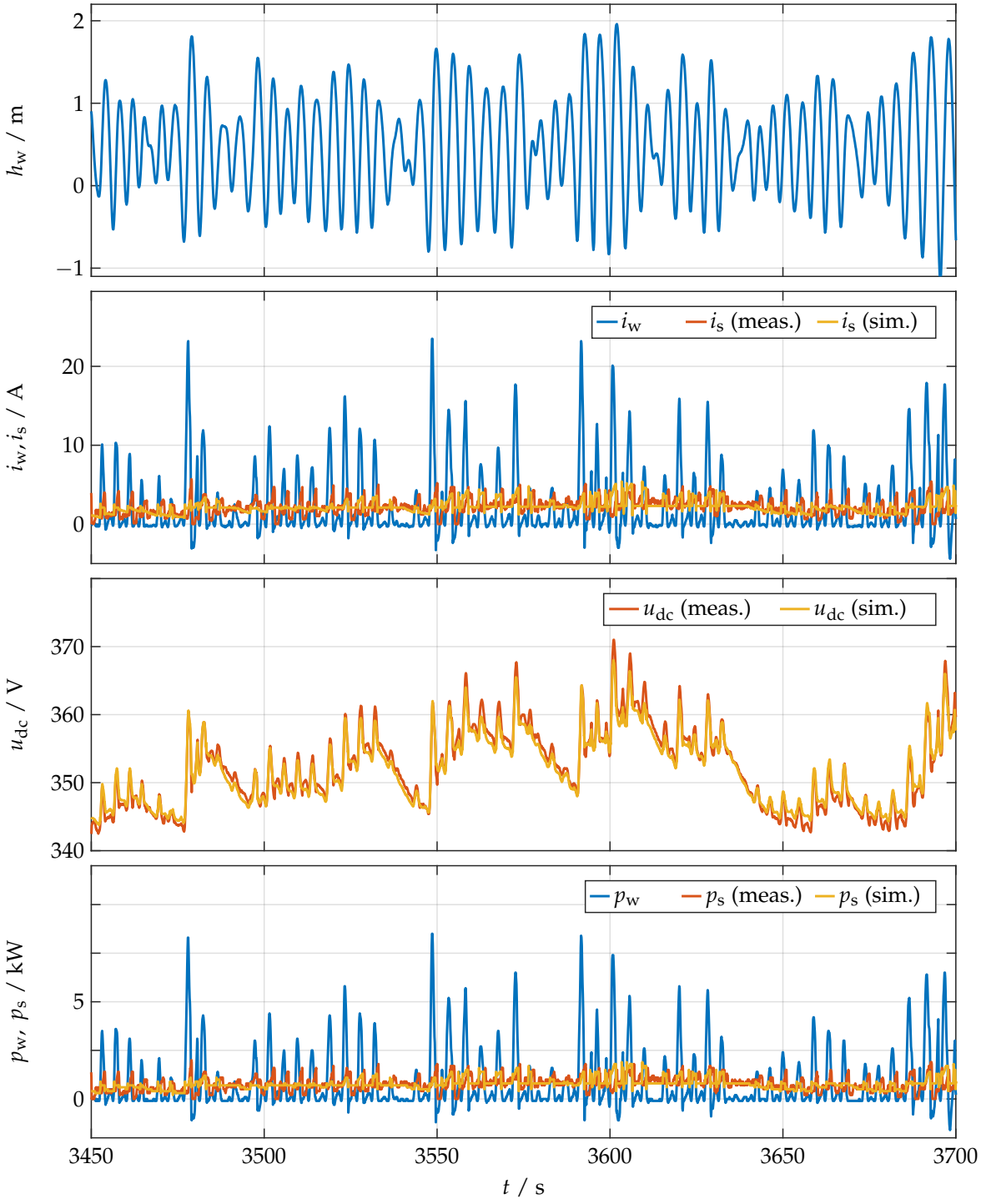

Figure 8. Comparison of the measured [——] and simulated [——] quantities of the DC-link control, with the rod position h_w at the top, followed by the current i_w and the smoothed current i_s, the DC-link voltage u_{dc} and the power of the generator units p_w and the smoothed power p_s. The measured current i_w and the power of the generator units p_w are used as inputs for the simulation [——].

The DC-link voltage u_{dc}, shown in the third subplot can be reproduced very well by the simulation. The average voltage is about the aimed 350 V, which is achieved

by the restoring component i_{res}, defined in Equation (15). The DC-link voltage can be used to determine the power generated. Each wave causes a high current flow into the supercapacitor bank, resulting in a voltage peak, induced by the ESR of the capacitors. Therefore, its modelling is especially important to calculate the reference voltage correctly. Disregarding these voltage peaks, there are grouped time intervals where more energy is generated than in others. This results from the tendency for larger waves to be grouped together, which is called wave groupiness ([1] Section 3.3.4), [47]. This can also be concluded from the movement of the lifting rod. Thus, power smoothing must not only smooth the power between two waves but also over these sets of waves for a longer period of time.

The resulting power p_{s} into the energy storage system is well smoothed, also over multiple sets of waves, as seen in the last subplot. This confirms that both the system parameters and the designed controller were chosen correctly and are working very well. Thus, the extended lifetime of the batteries can be guaranteed. Furthermore, the simulation can reproduce the measured quantities very well, which validates the used model and allows further development of the system.

6. Conclusions

The electrical system of a wave energy converter prototype was presented. To smooth the highly fluctuating power, generated by the waves' movements, a supercapacitor bank was directly connected to the DC-link. A unidirectional DC/DC converter was used to charge batteries from the DC-link.

To charge and discharge the supercapacitor bank during the period of a wave, the DC-link voltage must change, according to the fluctuating power. The DC-link voltage is controlled by the current through the DC/DC converter, where the reference current is computed in a PLC and transmitted to the converter. The control system is divided into two parts. The first part measures the generated power and calculates the reference DC-link voltage, yielding a nonlinear control system. The subsequent voltage control loop ensures that the DC-link voltage follows this reference. To prove a safe and stable operation, a stability analysis was conducted. The nonlinear dynamics were linearised around the operational point, yielding the small signal state space representation of the DC-link control system. Numerical analysis showed that the analysed system is exponentially stable.

The presented results in Section 5 show a nicely smoothed power. Under the given wave conditions, even the power fluctuation resulting from wave groupiness can be smoothed over multiple wave groups and a longer period of time, which indicates a proper system and controller design. The simulation results match the measurement results, on the bases of which further development can be initiated. As next steps, a bidirectional DC/DC converter shall be installed to connect the supercapacitor bank to the DC-link. This allows a more constant voltage in the DC-link, which is better for the control of the generator units and reduces the transmission losses. In addition, supercapacitors can be utilized more efficiently.

Author Contributions: Conceptualization, S.K. and C.M.H.; methodology, S.K. and C.M.H.; software, S.K.; validation, S.K. and C.M.H.; formal analysis, S.K. and C.M.H.; investigation, S.K.; resources, S.K. and C.M.H.; data curation, S.K.; writing—original draft preparation, S.K.; writing—review and editing, S.K. and C.M.H.; visualization, S.K.; supervision, C.M.H.; project administration, S.K. All authors have read and agreed to the published version of the manuscript.

Funding: This research received no external funding.

Institutional Review Board Statement: Not applicable.

Informed Consent Statement: Not applicable.

Data Availability Statement: Not applicable.

Conflicts of Interest: The authors declare no conflict of interest.

Nomenclature

$\mathbb{N}, \mathbb{R}$	natural and real numbers
$\boldsymbol{x} := (x_1, \ldots, x_n)^\top \in \mathbb{R}^n$	column vector, $n \in \mathbb{N}$ (where $:=$ means "is defined as" and $^\top$ means "transposed")
$\|\boldsymbol{x}\| := \sqrt{\boldsymbol{x}^\top \boldsymbol{x}}$	Eucilidean norm of $\boldsymbol{x}$
$\boldsymbol{A} \in \mathbb{R}^{n \times m}$	real matrix with n rows and m columns, n,$m \in \mathbb{N}$
$\boldsymbol{O}_{n \times m} \in \mathbb{R}^{n \times m}$	zero matrix
$\boldsymbol{I}_n := \mathrm{diag}(1, \ldots, 1) \in \mathbb{R}^{n \times n}$	identity matrix
x_{ref}	reference value of e.g., voltage, current and power
x_{nom}	nominal value of e.g., voltage, current and power
x_{max}	maximum value of e.g., voltage, current and power
x_{min}	minimum value of e.g., voltage, current and power
$\overline{x}$	average value of e.g., voltage, current and power
u_{dc}	DC-link voltage
$u_{\mathrm{bat}}, i_{\mathrm{bat}}$	battery voltage and current
$i_{\mathrm{w}}, p_{\mathrm{w}}$	current and power from the generator units
$i_{\mathrm{s}}, p_{\mathrm{s}}$	current and power flowing into the DC/DC converter
$\xi_{\mathrm{s,ref}}$	quantity, representing the integral action of the PI-controller
C	capacitance of the supercapacitor bank
R_{esr}	equivalent series resistors (ESR) of the supercapacitor bank
$u_{\mathrm{c}}, i_{\mathrm{c}}$	voltage and current of the capacitance
$u_{\mathrm{esr}}, p_{\mathrm{esr}}$	voltage and power of the ESR
E_{c}	stored energy in the supercapacitor bank
τ_{s}	time constant of the current dynamics of the DC/DC converter
τ_{w}	time constant of the low pass filter to filter p_{w}
$V_{\mathrm{r}}, \tau_{\mathrm{r}}$	parameter of the PI-controller
$i_{\mathrm{res}}, V_{\mathrm{res}}, f_{\mathrm{res}}$	restoring current, factor and frequency
$\boldsymbol{x}^\star := (u_{\mathrm{c}}^\star, i_{\mathrm{s}}^\star, \xi_{\mathrm{s,ref}}^\star, u_{\mathrm{c,ref}}^\star, \vec{i}_{\mathrm{w}}^\star)^\top$	quantity vector of the operation point

References

1. Pecher, A.; Kofoed, J. *Handbook of Ocean Wave Energy*; Springer: Cham, Switzerland, 2017. [CrossRef]
2. Kempener, R.; Neumann, F. *Ocean Energy Technology Brief*; Technical Report; IRENA—International Renewable Energy Agency: Abu Dhabi, United Arab Emirates, 2014.
3. Mørk, G.; Barstow, S.; Kabuth, A.; Teresa Pontes, M. Assessing the Global Wave Energy Potential. In Proceedings of the 29th International Conference on Ocean, Offshore Mechanics and Arctic, Shanghai, China, 6–11 June 2010; Volume 3. [CrossRef]
4. Reguero, B.G.; Losada, I.J.; Méndez, F.J. A global wave power resource and its seasonal, interannual and long-term variability. *Appl. Energy* **2015**, *148*, 366–380. [CrossRef]
5. Fairley, I.; Lewis, M.; Robertson, B.; Hemer, M.; Masters, I.; Horrillo-Caraballo, J.; Karunarathna, H.; Reeve, D.E. A classification system for global wave energy resources based on multivariate clustering. *Appl. Energy* **2020**, *262*, 114515. [CrossRef]
6. Yetkin, M.; Kalidoss, S.; Curtis, F.E.; Snyder, L.V.; Banerjee, A. Practical optimal control of a wave-energy converter in regular wave environments. *Renew. Energy* **2021**, *171*, 1382–1394. [CrossRef]
7. Rahm, M.; Svensson, O.; Bostrom, C.; Waters, R.; Leijon, M. Experimental results from the operation of aggregated wave energy converters. *IET Renew. Power Gener.* **2012**, *6*, 149–160. [CrossRef]
8. Sjolte, J.; Tjensvoll, G.; Molinas, M. Power Collection from Wave Energy Farms. *Appl. Sci.* **2013**, *3*, 420–436. [CrossRef]
9. Bailey, H.; Robertson, B.; Ortiz, J.; Buckham, B. Stochastic Methods to Predict WEC Array Power for Grid Integration. In Proceedings of the 11th European Wave and Tidal Energy Conference, Nantes, France, 6–11 September 2015.
10. Göteman, M.; Engström, J.; Eriksson, M.; Isberg, J.; Leijon, M. Methods of reducing power fluctuations in wave energy parks. *J. Renew. Sustain. Energy* **2014**, *6*, 043103. [CrossRef]
11. Astariz, S.; Iglesias, G. Output power smoothing and reduced downtime period by combined wind and wave energy farms. *Energy* **2016**, *97*, 69–81. [CrossRef]
12. Veigas, M.; Iglesias, G. A Hybrid Wave-Wind Offshore Farm for an Island. *Int. J. Green Energy* **2015**, *12*, 570–576. [CrossRef]
13. Gao, Q.; Ding, B.; Ertugrul, N.; Li, Y. Impacts of mechanical energy storage on power generation in wave energy converters for future integration with offshore wind turbine. *Ocean Eng.* **2022**, *261*, 112136. [CrossRef]

14. Santos, M.; Salcedo, F.; Haim, D.B.; Mendia, J.L.; Ricci, P.; Villate, J.; Khan, J.; Leon, D.; Arabi, S.; Moshref, A.; et al. *Integrating Wave and Tidal Current Power: Case Studies Through Modelling and Simulation*; Research Report Document No: T0331; International Energy Agency Implementing Agreement on Ocean Energy Systems: Paris, France, 2011.
15. Blavette, A.; O'Sullivan, D.L.; Lewis, A.W.; Egan, M.G. Impact of a wave farm on its local grid: Voltage limits, flicker level and power fluctuations. In Proceedings of the 2012 Oceans-Yeosu, Yeosu, Korea, 21–24 May 2012; pp. 1–9. [CrossRef]
16. Murray, D.B.; Egan, M.G.; Hayes, J.G.; O'Sullivan, D.L. Applications of Supercapacitor Energy Storage for a Wave Energy Converter System. In Proceedings of the 8th European Wave and Tidal Energy Conference, Uppsala, Sweden, 7–11 September 2009.
17. Barelli, L.; Bidini, G.; Ciupageanu, D.; Ottaviano, A.; Pelosi, D.; Gallorini, F.; Alessandri, G.; Atcheson Cruz, M. An effective solution to boost generation from waves: Benefits of a hybrid energy storage system integration to wave energy converter in grid-connected systems. *Open Res. Eur.* **2022**, *2*, 40. [CrossRef]
18. Glavin, M.E.; Chan, P.K.W.; Armstrong, S.; Hurley, W.G. A stand-alone photovoltaic supercapacitor battery hybrid energy storage system. In Proceedings of the 2008 13th International Power Electronics and Motion Control Conference, Poznan, Poland, 1–3 September 2008; pp. 1688–1695. [CrossRef]
19. Burke, A. Ultracapacitors: Why, how, and where is the technology. *J. Power Sources* **2000**, *91*, 37–50. [CrossRef]
20. Lijun Gao, R.A.D.; Liu, S. Power Enhancement of an Actively Controlled Battery/Ultracapacitor Hybrid. *IEEE Trans. Power Electron.* **2005**, *20*, 236–243. [CrossRef]
21. Abbey, C.; Joos, G. Supercapacitor Energy Storage for Wind Energy Applications. *IEEE Trans. Ind. Appl.* **2007**, *43*, 769–776. [CrossRef]
22. Li, W.; Joos, G.; Abbey, C. A Parallel Bidirectional DC/DC Converter Topology for Energy Storage Systems in Wind Applications. In Proceedings of the 2007 IEEE Industry Applications Annual Meeting, New Orleans, LA, USA, 23–27 September 2007; pp. 179–185. [CrossRef]
23. Falcão, A.O. Control of an oscillating-water-column wave power plant for maximum energy production. *Appl. Ocean Res.* **2002**, *24*, 73–82. [CrossRef]
24. Yoshida, T.; Sanada, M.; Morimoto, S.; Inoue, Y. Study of Flywheel Energy Storage System for Power Leveling of Wave Power Generation System. In Proceedings of the 2012 15th International Conference on Electrical Machines and Systems (ICEMS), Sapporo, Japan, 21–24 October 2012; pp. 1–5.
25. Nie, Z.; Xiao, X.; Kang, Q.; Aggarwal, R.; Zhang, H.; Yuan, W. SMES-Battery Energy Storage System for Conditioning Outputs From Direct Drive Linear Wave Energy Converters. *IEEE Trans. Appl. Supercond.* **2013**, *23*, 5000705. [CrossRef]
26. Zhou, Z.; Benbouzid, M.; Charpentier, J.F.; Scuiller, F.; Tang, T. A review of energy storage technologies for marine current energy systems. *Renew. Sustain. Energy Rev.* **2013**, *18*, 390–400. [CrossRef]
27. Aubry, J.; Bydlowski, P.; Multon, B.; Ben Ahmed, H.; Borgarino, B. Energy Storage System Sizing for Smoothing Power Generation of Direct Wave Energy Converters. In Proceedings of the 3rd International Conference on Ocean Energy, Bilbao, Spain, 6 October 2010; ISBN 978-84-693-5467-4.
28. Moreno-Torres, P.; Blanco, M.; Navarro, G.; Lafoz, M. Power Smoothing System for Wave Energy Converters by means of a Supercapacitor-Based Energy Storage System. In Proceedings of the 17th European Conference on Power Electronics and Applications (EPE'15 ECCE-Europe), Geneva, Switzerland, 8–10 September 2015; pp. 1–9. [CrossRef]
29. Nie, Z.; Xiao, X.; Hiralal, P.; Huang, X.; McMahon, R.; Zhang, M.; Yuan, W. Designing and Testing Composite Energy Storage Systems for Regulating the Outputs of Linear Wave Energy Converters. *Energies* **2017**, *10*, 114. [CrossRef]
30. Rajapakse, G.; Jayasinghe, S.; Fleming, A.; Negnevitsky, M. Grid Integration and Power Smoothing of an Oscillating Water Column Wave Energy Converter. *Energies* **2018**, *11*, 1871. [CrossRef]
31. Navarro, G.; Blanco, M.; Torres, J.; Nájera, J.; Santiago, A.; Santos-Herran, M.; Ramírez, D.; Lafoz, M. Dimensioning Methodology of an Energy Storage System Based on Supercapacitors for Grid Code Compliance of a Wave Power Plant. *Energies* **2021**, *14*, 985. [CrossRef]
32. Masuda, A.; Goto, H. Control Strategy for Power Smoothing Converter with Energy Storage for Maximum Power Controlled Wave Energy Converter. In Proceedings of the 2021 10th International Conference on Renewable Energy Research and Application (ICRERA), Ankara, Turkey, 26–29 September 2021; pp. 235–238. [CrossRef]
33. Krüner, S.; Hackl, C.M. Experimental Identification of the Optimal Current Vectors for a Permanent-Magnet Synchronous Machine in Wave Energy Converters. *Energies* **2019**, *12*, 862. [CrossRef]
34. Maxwell Technologies. *BC Series Ultracapacitors-BCAP0350*. Datasheet. Available online: https://maxwell.com/products/ultracapacitors/cells/(accessed on 22 October 2022).
35. Linzen, D.; Buller, S.; Karden, E.; De Doncker, R.W. Analysis and Evaluation of Charge-Balancing Circuits on Performance, Reliability, and Lifetime of Supercapacitor Systems. *IEEE Trans. Ind. Appl.* **2005**, *41*, 1135–1141. [CrossRef]
36. Diab, Y.; Venet, P.; Rojat, G. Comparison of the Different Circuits Used for Balancing the Voltage of Supercapacitors: Studying Performance and Lifetime of Supercapacitors. ESSCAP; HAL: Lausanne, Switzerland, 2006.
37. Shi, L.; Crow, M.L. Comparison of Ultracapacitor Electric Circuit Models. In Proceedings of the 2008 IEEE Power and Energy Society General Meeting—Conversion and Delivery of Electrical Energy in the 21st Century, Pittsburgh, PA, USA, 20–24 July 2008; pp. 1–6. [CrossRef]
38. Fletcher, S.; Kirkpatrick, I.; Dring, R.; Puttock, R.; Thring, R.; Howroyd, S. The modelling of carbon-based supercapacitors: Distributions of time constants and Pascal Equivalent Circuits. *J. Power Sources* **2017**, *345*, 247–253. [CrossRef]

39. Daratha, N.; Polinder, H.; de Sousa Prado, M. A first-order energy storage requirements estimation for an Archimedes Wave Swing Park. In Proceedings of the 2008 IEEE International Conference on Sustainable Energy Technologies, Singapore, 24–27 November 2008; pp. 1161–1165. [CrossRef]
40. Wu, E.; Knight, A.M. Considerations for sizing energy storage technologies in wave energy systems. In Proceedings of the 2017 20th International Conference on Electrical Machines and Systems (ICEMS), Sydney, Australia, 11–14 August 2017; pp. 1–6. [CrossRef]
41. Francesco Di Domenico, Alois Steiner, J.C. *Design of a 600 W HB LLC Conver ter Using 600 V CoolMOS^{TM} P6*; Technical Report; Infinion: Singapore, 2015.
42. Studer Innotec. VarioString VS-70. Datasheet. Available online: https://www.studer-innotec.com/de/produkt-details/variostring-reihe/vs-70-313 (accessed on 22 October 2022).
43. *IEEE Std 1561-2019 (Revision of IEEE Std 1561-2007)*; IEEE Guide for Optimizing the Performance and Life of Lead-Acid Batteries in Remote Hybrid Power Systems. IEEE: New York, NY, USA, 2019, pp. 1–34. [CrossRef]
44. Hackl, C.M. *Non-identifier Based Adaptive Control in Mechatronics: Theory and Application*; Springer International Publishing: Basel, Switzerland, 2017.
45. Schröder, D.; Böcker, J., Eds. *Elektrische Antriebe–Regelung von Antriebssystemen*; Springer: Berlin/Heidelberg, Germany, 2020. [CrossRef]
46. Ludyk, G. *Theoretische Regelungstechnik 1*; Springer: Berlin/Heidelberg, Germany, 1995.
47. List, J.H. Wave groupiness variations in the nearshore. *Coast. Eng.* **1991**, *15*, 475–496. [CrossRef]